communications materials

Article

https://doi.org/10.1038/s43246-024-00503-6

3D printed titanium carbide MXene-coated polycaprolactone scaffolds for guided neuronal growth and photothermal stimulation

Check for updates

Jianfeng Li[1,2], Payam Hashemi[1,3], Tianyi Liu[1,4], Ka My Dang[1,2], Michael G. K. Brunk[1,2], Xin Mu[1,4], Ali Shaygan Nia[1,3], Wesley D. Sacher[1,2], Xinliang Feng[1,3] & Joyce K. S. Poon[1,2,4]

The exploration of neural circuitry is paramount for comprehending the computational mechanisms and physiology of the brain. Despite significant advances in materials and fabrication techniques, controlling neuronal connectivity and response in 3D remains a formidable challenge. Here, we introduce a method for engineering the growth of 3D neural circuits with the capability for optical stimulation. We fabricate bioactive interfaces by melt electrospinning writing (MEW) 3D polycaprolactone (PCL) scaffolds followed by coating with titanium carbide ($Ti_3C_2T_x$ MXene). Beyond enhancing hydrophilicity, cell adhesion, and electrical conductivity, the $Ti_3C_2T_x$ MXene coating enables optocapacitance-based neuronal stimulation, induced by localized temperature increases upon illumination. This approach offers a pathway for additive manufacturing of neural tissues endowed with optical control, facilitating functional tissue engineering and neural circuit computation.

Deciphering neuronal activity in the brain is a longstanding and formidable challenge, holding significant implications ranging from advancements in computer architecture to clinical breakthroughs[1]. Neural circuits and synaptic connectivity constitute the fundamental building blocks of neural functionality[2]. Understanding the intricacies of brain circuitry not only inspires ways to enhance computational efficiency[3], but also provides invaluable insights into neurological disorders and pharmaceutical screening[4]. However, investigations in neural circuits in vivo or ex vivo are subjected to regulatory constraints and the complexities of biological brain structures[5]. In vitro neural circuit models can serve as simplified platforms for investigating neural functions at the cellular level to reduce the need for animal models. Although in vitro two-dimensional (2D) neural circuit engineering can be achieved by manipulating the surfaces in cell cultures[6], this fails to fully recapitulate the three-dimensional (3D) characteristics of the in vivo neuronal microenvironment. Various techniques, including microfluidics[7], electrocompaction[8], photolithography[9], colloids[10], and superparamagnetic nanoparticles[11], have been employed for engineering 3D neural circuits, but these methods lack precise control over structural and cellular details, limiting their suitability for manipulating neural circuits at the single-cell level. 3D printing can also enable the engineering of 3D neural circuits, but current 3D-printed neural circuit scaffolds either exhibit large millimeter-scale feature sizes[12] or require complex synthetic modifications of biological cues[13].

The precise modulation of neuronal activity within a circuit is critical to the comprehensive investigation of neural circuit function[14]. Optogenetics and multielectrode arrays (MEAs) are key technologies for neural stimulation and readout in cultures[15,16]. However, optogenetics encounters challenges such as variable transfection efficiency and clinical approvals, while MEAs have limited spatial resolution in recording/stimulation and do not match the mechanical properties of tissues[17,18]. The optocapacitive effect, the change in the cell membrane capacitance due to light-induced localized heating of the neurons, is an emerging approach for neuron stimulation without the need for genetic modifications and device transplantation[19–21]. Laser pulses can stimulate action potentials, but the optical energies and intensities must be kept sufficiently low to avoid damaging the tissue. The optical intensity for photodamage or phototoxicity in cells is substantially higher for red light (wavelength near 640 nm) than at blue, green, and ultraviolet wavelengths[22–24]. Wäldchen et al.[22] show that intensity limit of

[1]Max Planck Institute of Microstructure Physics, Halle, Germany. [2]Max Planck-University of Toronto Centre for Neural Science and Technology, Toronto, ON, Canada. [3]Faculty of Chemistry and Food Chemistry & Center for Advancing Electronics Dresden, Technische Universität Dresden, Dresden, Germany. [4]Department of Electrical and Computer Engineering, University of Toronto, Toronto, ON, Canada. e-mail: jianfeli@mpi-halle.mpg.de; joyce.poon@mpi-halle.mpg.de

photodamage is in excess of 10 MW m^{-2} for a wavelength of 640 nm, while Emon et al.[23] recommends 57 W m^{-2} as a safe threshold for cell force homeostasis and Dubois et al.[24] observed that 0.2 MW m^{-2} did not cause cellular damage in tissues. To stimulate with lower pulse energies and high spatial specificity, light absorbing particles, such as 3D fuzzy graphene[25], transition metal carbide/nitride (MXene) flakes[26], as well as gold or carbon nanoparticles[19], are incorporated onto the neurons to increase the photothermal conversion efficiency in localized regions of the cells. In this way, neurons can be stimulated at the μm and millisecond (ms) spatial and temporal scales. However, the application of these materials has been largely limited to 2D systems or single-cell studies, rather than to 3D structures.

In this work, we present $Ti_3C_2T_x$ MXene-coated 3D polycaprolactone (PCL) scaffolds fabricated using melt electrospinning writing (MEW) with micrometer-scale features for optocapacitive neuron stimulation. Cell culture interfaces strongly influence cell properties such as cell adhesion, morphology, migration, and intercellular communication[27]. Therefore, bioactive interfaces can guide neuronal growth cones and the interconnection of neurons, enabling the controlled formation of neural circuits. $Ti_3C_2T_x$ MXene is an attractive material for bioactive neural interfaces due to its biocompatibility and capability of inducing strong photothermal effects. This is attributed to its high optical absorption of near-infrared wavelengths, which is enhanced by the excitation of localized surface plasmons[28,29]. $Ti_3C_2T_x$ MXene has been used as a coating for cell culture substrates and as a medium suspension for dorsal root ganglion cell culture and stimulation[26]. However, these investigations have been limited to 2D systems and did not explore neuronal interconnection. Additionally, $Ti_3C_2T_x$ MXene coating can confer bioinert electrospun PCL conduits with excellent biocompatibility in vitro and in vivo, thereby facilitating physiological electrical signal transmission and promoting angiogenesis[30]. Our $Ti_3C_2T_x$ MXene-coated PCL scaffolds were effective in controlling neuronal interconnection, demonstrating their potential in regulating neuronal network formation and activity.

Results and discussion

3D fabrication of $Ti_3C_2T_x$/PCL scaffolds

Figure 1 shows an overview of the 3D $Ti_3C_2T_x$/PCL scaffold neural interface. The $Ti_3C_2T_x$ MXene serves as a surface modification for the 3D printed PCL scaffolds. Neuron growth is guided along the scaffold and the enables optical stimulation. PCL was selected as the substrate material because it is approved by the Food and Drug Administration (FDA) and has been explored extensively in tissue engineering for its ease of processing, biocompatibility, controllable biodegradation[31]. In the initial step, PCL scaffolds were fabricated through MEW-based 3D printing, achieving high-resolution structures with micrometer-scale features. This approach avoids the use of toxic solvents that may compromise the cytocompatibility of the supportive structures. Subsequently, pristine PCL scaffolds were coated with $Ti_3C_2T_x$ MXene via drop casting and self-assembly, using a similar method as reported before[32]. The $Ti_3C_2T_x$ MXene coating introduces extensive oxygen/fluorine-containing groups to the hydrophobic PCL surface, promoting cellular protrusion attachment[33]. Combined with the precisely defined microscale geometry, the 3D $Ti_3C_2T_x$/PCL scaffold provides guidance for neurons to grow and form interconnected networks.

Characterization of $Ti_3C_2T_x$ MXene and 3D fabricated scaffolds

To prepare $Ti_3C_2T_x$ MXene, the Al layer in the precursor Ti_3AlC_2 MAX phase (Fig. 2a) was selectively etched away by hydrofluoric acid (HF), as described in the experimental section, to obtain the $Ti_3C_2T_x$ MXene particles with the so-called accordion-like multilayer structures (Fig. 2b). Surface terminal groups such as fluorine (–F), oxygen (–O, =O), and hydroxyl (–OH) are introduced during the removal of the Al layers by etching with HF[34]. More specifically, the fluorine atoms are arranged in atom thin strips with orderly connections adjacent to oxygen containing groups, showing no phase separation or agglomeration[35]. Ti-O-F bonds and F-C bonds are the most abundant fluorine containing bonding after HF treatment[36]. These surface terminal atoms and groups are responsible for the hydrophilicity of the MXene. With subsequent treatment, delaminated $Ti_3C_2T_x$ MXene was obtained (Fig. 2c). Analysis of the X-ray diffraction (XRD) patterns revealed that the (002) peak, corresponding to the crystallographic plane of MXene, remained as the prominent peak following the etching, intercalation, and delamination treatment of the MAX phase (Fig. 2d). This observation suggests the successful removal of other components from the MAX phase. Furthermore, the broadening and shifting of the (002) peak from the MAX phase to MXene indicate a reduced thickness of the $Ti_3C_2T_x$ MXene layer and an increased d-spacing[37]. The resulting aqueous dispersion of MXene was employed for the coating of the PCL scaffold in the next steps.

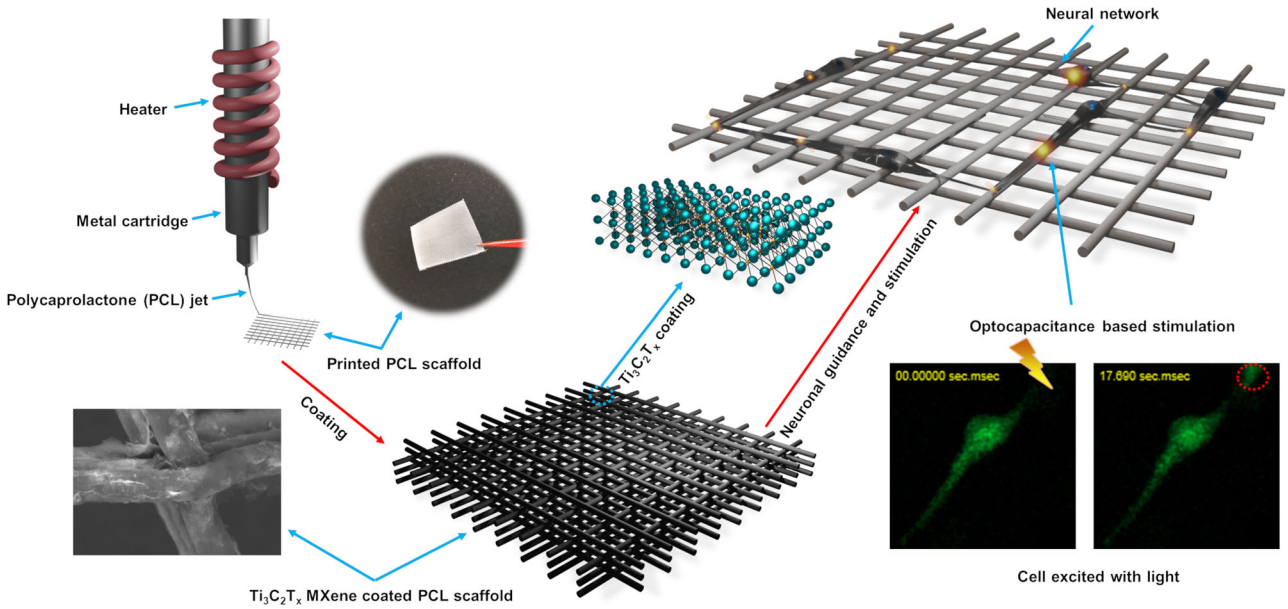

Fig. 1 | Schematic illustration of 3D fabrication of $Ti_3C_2T_x$/PCL scaffold as neural network guidance and addressable optical stimulation platform. Mechanically robust PCL scaffolds were printed with the well-controlled PCL jet from the heated cartridge and $Ti_3C_2T_x$ coating formed uniformly on the pristine PCL scaffold surface to render a cell friendly biointerface, which could be used to increase the effectiveness of optocapacitance based neuronal stimulation.

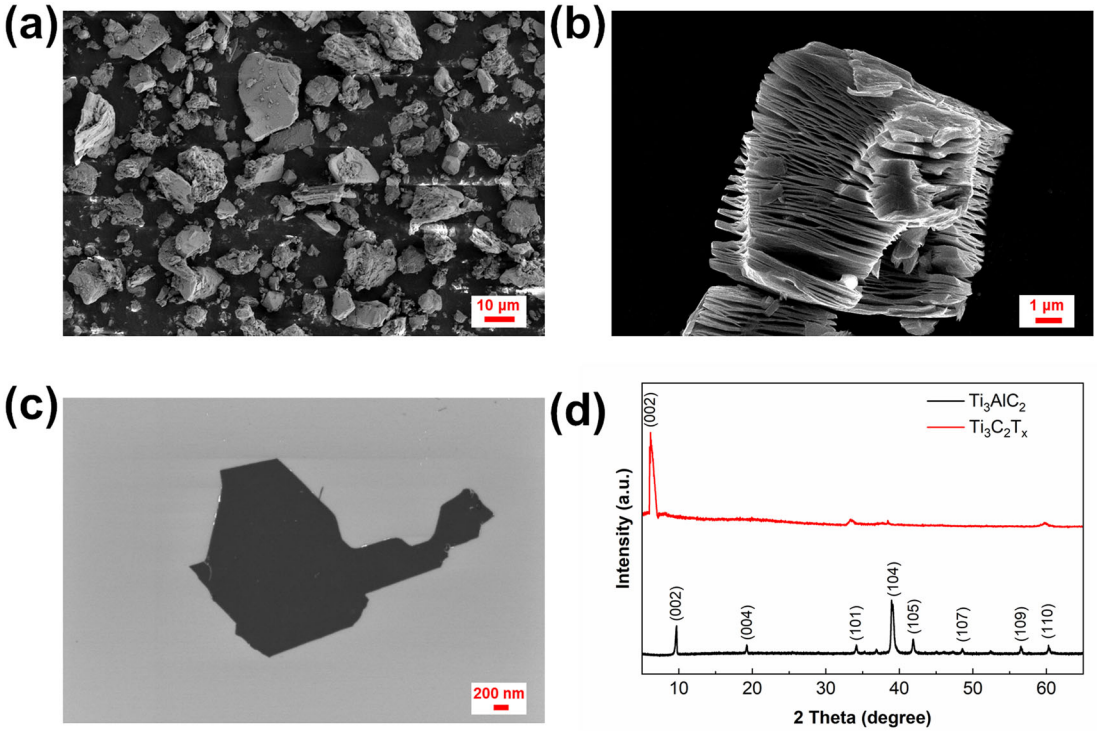

Fig. 2 | $Ti_3C_2T_x$ MXene characterization. Scanning electron microscope (SEM) images of **a** Ti_3AlC_2 (MAX phase) powder particles (precursor of MXene), **b** multilayer $Ti_3C_2T_x$ (MXene particle) after etching away the Al layer, and **c** delaminated $Ti_3C_2T_x$ MXene flake. X-ray diffraction (XRD) patterns of the **d** Ti_3AlC_2 MAX phase and $Ti_3C_2T_x$ MXene.

Electrospinning is effective for fabricating one-dimensional (1D) and 2D nano/micro-fibrous structures, with applications in numerous research domains, including biomedical engineering[38]. However, a challenge in electrospinning is the control over the generated fibers due to the chaotic motion of materials in the fabrication process[39]. To address this issue, MEW-based 3D printing was developed by placing the fluid jet onto the programmable motorized collector before the Plateau–Rayleigh instability criterion applies to the ejected fiber to attain accurate material deposition with high single fiber resolution[40]. With well-tuned MEW parameters, a 7-mm-thick printed construct can be formed with well-defined fiber placement and overall geometry[41]. Besides printing fine well-aligned straight fibers, MEW can also generate curved or coiled fibers when operating below the critical translation speed (CTS) and produce thinned fibers or beads above CTS[42]. MEW provides more control over the final geometry of the fibrous scaffolds than the conventional technology (i.e., depositing fibers without control and forming random pores)[42], enabling free infiltration of live cells through the structure. With the continual advancements, MEW can enable new possibilities for tissue engineering applications.

In our study, with precisely tuned parameters, 3D PCL scaffolds were fabricated by MEW with well-defined geometry and desirable morphology (Fig. 3a and Supplementary Movie 1). Despite the delicate and fibrous nature of the printed structure, 3D printed PCL scaffold with more layers were sufficiently robust to be handled with tweezers (Supplementary Fig. 1). Since PCL is hydrophobic[43], the 3D printed pristine PCL scaffolds with different strand distances (SDs) of 200, 100, and 50 μm (measured from the center of the strands) exhibited poor wettability of water with corresponding contact angles of $127.40 \pm 4.12°$ ($n = 3$), $134.92 \pm 2.02°$ ($n = 3$), and $133.36 \pm 0.97°$ ($n = 3$), respectively (Fig. 3a). Compared to the 3D printed PCL scaffolds, the water droplet contact angles are significantly larger than those on a clean glass slide [$14.85 \pm 2.49°$ ($n = 3$)] (Supplementary Fig. 2), which is detrimental for applications in water-based systems. However, a solution of 70% ethanol/water (70% EtOH; v/v) could spread throughout the structure, which eliminated the electrostatic attraction between the scaffold and the glass, causing the scaffold to detach from glass substrate (Supplementary Movie 2). Materials with low wettability, such as hydrophobic materials, exhibit limited cell adhesion and fail to provide the necessary environment for cellular growth and development[44]. To modify the wettability of PCL, we coated the structures with $Ti_3C_2T_x$ MXene, which is hydrophilic due to abundant oxygen and fluorine functional groups on its surface.

We printed PCL scaffolds with random distribution of pore sizes ranging from 1 to 50 μm to investigate the impact of $Ti_3C_2T_x$ MXene dispersion concentration and coating time on the resulting morphology of the coated structures. $Ti_3C_2T_x$ MXene dispersions in 70% EtOH, at concentrations of 0.5, 1.5, and 3.0 mg mL^{-1}, were successfully and uniformly deposited onto the 3D printed PCL scaffolds with only minimal blockages observed in small pores (Supplementary Fig. 3). However, when a highly concentrated $Ti_3C_2T_x$ MXene dispersion (15.0 mg mL^{-1}) in water was used for coating, it resulted in the partial blockage of nearly all pores after a single coating, and subsequent coating led to the formation of a film covering the entire scaffold (Supplementary Fig. 3). This phenomenon can be attributed to the high viscosity of the concentrated dispersion and poor wettability during the coating process without the presence of ethanol. Furthermore, increasing the MXene concentration and the number of coating times led to lower electrical sheet resistance (Supplementary Fig. 4), as more interconnected conductive pathways were formed in the plane of the MXene structures[45]. For instance, the sheet resistance of 3-time coated PCL structure with 15.0 mg mL^{-1} MXene solution reached ~18 $\Omega\,\square^{-1}$, comparable to the 5-μm-thick $Ti_3C_2T_x$ MXene membrane reported in previous research[46]. The sheet resistance of the 3-time coated PCL structure with 3.0 mg mL^{-1} MXene dispersion was about 811 $\Omega\,\square^{-1}$, and the structures preserved good morphology with minimal blockage of the pores (Supplementary Fig. 3). The electrical conductivity of these structures, along with the well-coated MXene structures on the 3D printed PCL scaffolds, are favorable properties for applications to cell cultures[47]. Additionally, we studied the wettability of $Ti_3C_2T_x$ MXene coating on 3D printed PCL scaffolds with 100 μm SD. The $Ti_3C_2T_x$ MXene-coated PCL scaffolds showed favorable wettability (Supplementary Movie 3), with water droplet completely spreading into the

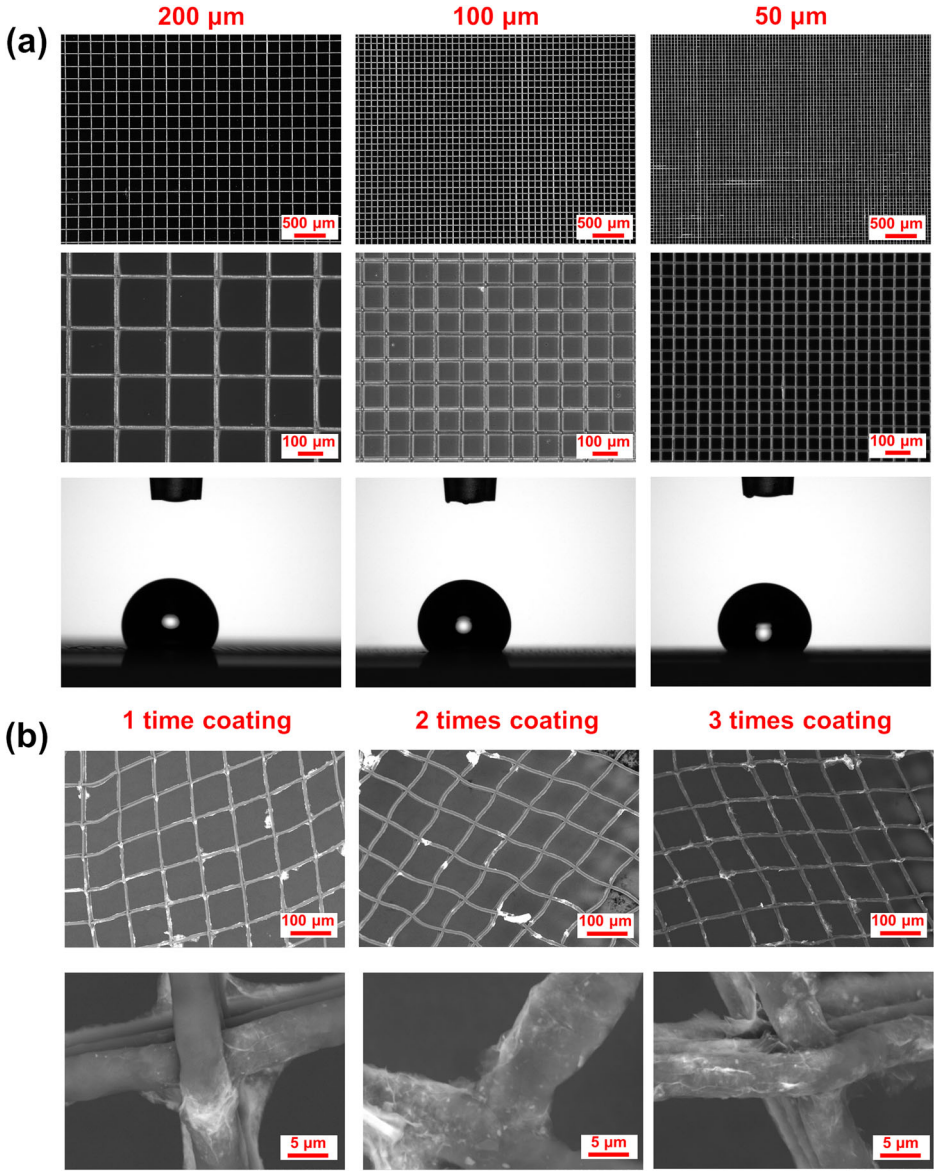

Fig. 3 | Characterization of 3D printed PCL and $Ti_3C_2T_x$/PCL scaffolds. a Optical microscopy images of 3D-printed PCL scaffolds with different strand distances (SDs) (200, 100, and 50 μm) and corresponding water droplet profiles on the structures. **b** SEM images of 3D $Ti_3C_2T_x$/PCL scaffolds with different coating times (1–3) at low and high magnifications.

coated structure within 1 min. The average diameter of deposited fiber was 5.75 ± 0.33 μm (n = 10), which is smaller than the diameter of neuronal cells, thereby allowing single cell attachment on the strands to facilitate the formation of precise cellular networks. When the MXene EtOH dispersion was applied to the pristine PCL scaffolds, the dispersion wetted the scaffolds easily, and the positively charged PCL surface attracted the negatively charged MXene flakes, resulting in uniform coatings on the scaffold[48,49]. As shown in Fig. 3b, 3D MXene/PCL scaffolds exhibited good overall morphology without altering the original design of the substrate structure and MXene coatings showed improved coverage with an increasing number of coatings as shown in the zoomed in SEM images (The enhanced coverage is indicated by a large number of layer in the MXene coatings and bright dot features on the coating layers.). Furthermore, as shown in Supplementary Fig. 5, energy dispersive X-ray (EDX) imaging confirms that more coating times result in a higher presence of the feature element for MXene (Ti). This also explains the lower electrical resistance as the number of coating layers increases (Supplementary Fig. 4). The mechanical properties of scaffolds play a pivotal role in tissue engineering. While the microscale mechanical properties of individual MXene nanoflakes are indeed exceptional, ranging from 670 MPa to 140 GPa[50], freestanding MXene films exhibit relatively low tensile strength, measuring only 3.5 MPa[51]. This discrepancy in strength arises from the loose interactions between different MXene sheets[51]. The inherently "soft" nature of MXene layered structures on the MXene/PCL scaffold may prove advantageous for cells originating from soft tissues or organs.

Neuronal behavior on the 3D $Ti_3C_2T_x$/PCL scaffold

Due to the low interfacial free energy and bioinert surface chemistry of PCL scaffold, cells have limited adhesion on the structure, resulting in reduced controllability over tissue regeneration[52]. With the bioactive functional groups on the surface of PCL scaffold introduced by efficient $Ti_3C_2T_x$ MXene coating, cell adhesion on the surface increased significantly after 1 day in culture, as shown in the fluorescence images in Fig. 4. Generally, more cells adhered and are distributed on the scaffold surface with $Ti_3C_2T_x$ MXene coatings formed from higher concentrations of $Ti_3C_2T_x$ MXene dispersions. $Ti_3C_2T_x$/PCL scaffolds with 15.0 mg mL^{-1} $Ti_3C_2T_x$ MXene dispersion coating had the densest cell population since the $Ti_3C_2T_x$ MXene could block the pores and provide more adhering points for cells compared to scaffolds coated with diluted $Ti_3C_2T_x$ MXene dispersions (Supplementary Fig. 3). Only a small number of cells adhered to the pristine PCL scaffold, and those cells showed rounded morphology and a lack of interaction with other cells through cilia, as shown in the SEM images in Fig. 4. In

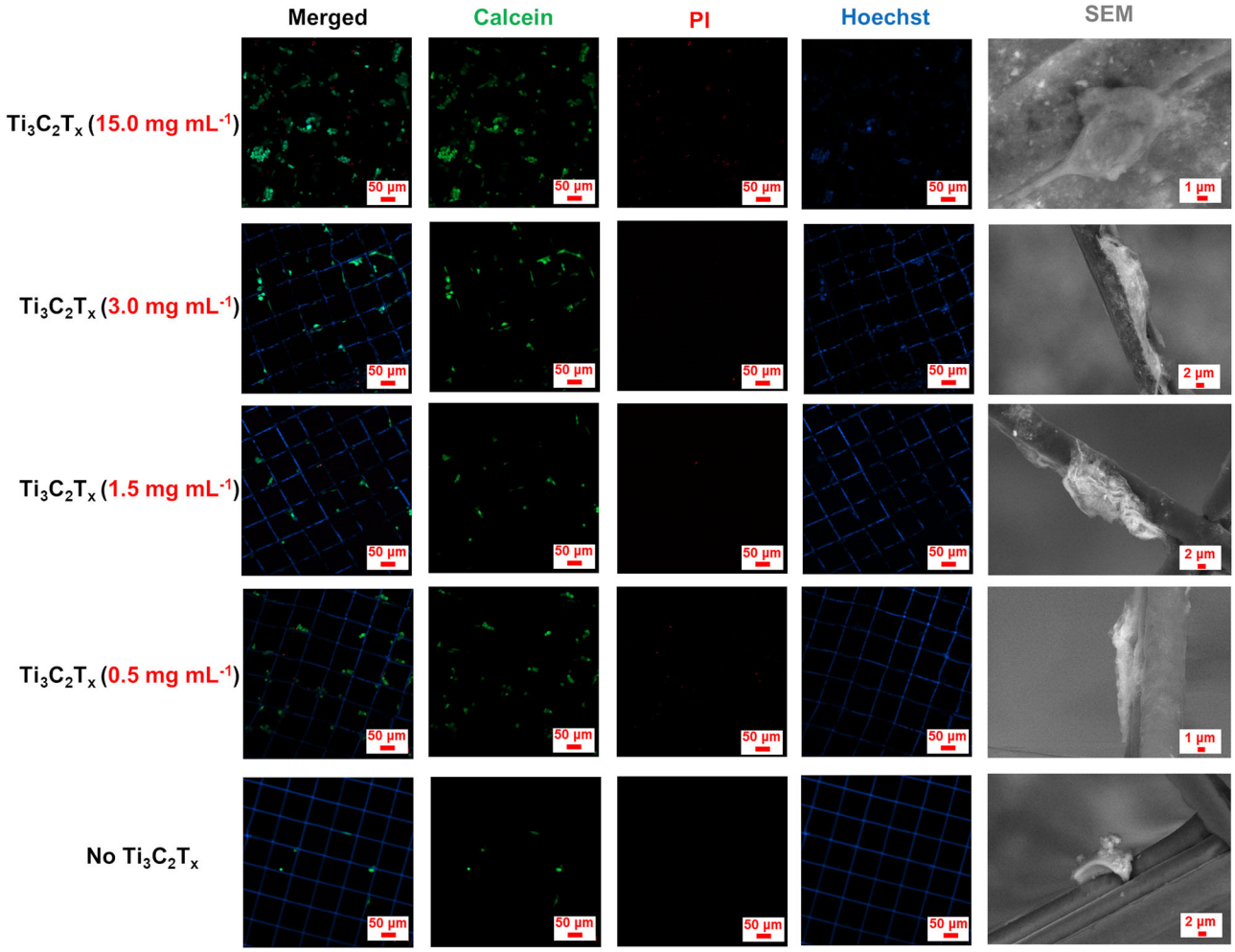

Fig. 4 | Cell viability and adhesion on 3D printed PCL scaffolds with and without $Ti_3C_2T_x$ MXene coatings. Fluorescence images of cell adhesion and morphology on $Ti_3C_2T_x$/PCL scaffolds with different coating concentrations of $Ti_3C_2T_x$ MXene dispersions after 1 day of culture, followed by corresponding SEM images. Live cell (Calcein; green), dead cell [propidium iodide (PI); red] and cell nucleus with PCL substrate (Hoechst; blue).

contrast, on the $Ti_3C_2T_x$ MXene-coated scaffolds, the cells showed elongated morphology with extended filopodia, spreading along the scaffolds. These results indicate that $Ti_3C_2T_x$ MXene coating efficiently increased the bioactivity of a bioinert material surface and promoted synaptic connectivity.

Figure 5 shows the morphology analysis of the neurons on the scaffolds. The results again show that without the coating of $Ti_3C_2T_x$ MXene, cells cultured on the pristine PCL scaffold exhibited a rounded morphology following seeding, whereas cells on $Ti_3C_2T_x$/PCL demonstrated an elongated morphology with extended filopodia, as observed in the immunofluorescence image (Fig. 5a). Subsequent exposure to retinoic acid for 3 days resulted in the differentiation of cells on both substrates into dopaminergic lineage, characterized by elongated cell morphology (Fig. 5b). However, on the pristine PCL substrate, no interconnected neurons were observed, whereas multiple interconnected neurons grew along the $Ti_3C_2T_x$/PCL, exhibiting significantly higher expression of F-actin and the neuronal marker β-tubulin III compared to cells on pristine PCL at Day 3, as well as both cultures at Day 1. As both F-actin and β-tubulin III are crucial proteins involved in neural growth signaling and navigation[53], the elevated expression of these proteins in cells on $Ti_3C_2T_x$/PCL could be attributed to enhanced neuronal growth and interaction. Neuronal somata adhered to the $Ti_3C_2T_x$/PCL scaffold interface conformally and growth cones grew alongside the scaffold (Fig. 5c). Eventually, they formed synaptic connections (Fig. 5d). The calcium oscillation of neurons on the $Ti_3C_2T_x$/PCL scaffold could be observed, indicating the active synaptic connections between neurons (Supplementary Movie 4). Thus, the physicochemical interaction between cells and the $Ti_3C_2T_x$ MXene coating also improved the interface for dopaminergic neuron differentiation and the formation of inter-neuronal circuits in our 3D structures.

The cytocompatibility of the $Ti_3C_2T_x$/PCL scaffolds was evaluated following a 7-day culture. As shown in Fig. 6, $Ti_3C_2T_x$ MXene coating exhibited excellent cytocompatibility for neuronal cultures with a viability of 92.1 ± 4.7%, significantly higher than that of the pristine PCL scaffold (76.7 ± 6.1%) (Supplementary Fig. 6). The SD of the printed scaffolds had an impact on neuronal growth and interconnection (Fig. 6 and Supplementary Fig. 7). More specifically, neurons did not strictly align along the scaffold strands during growth when the SD was smaller than 50 μm. This deviation from the anticipated growth pattern may have arisen from the interaction between growth cones of adjacent neurons when they were in close spatial proximity (Fig. 5a–d). In contrast, when the SD exceeded 100 μm, neurons adhered to the growth guidance provided by the scaffold strands, even as cellular multiplication occurred. This observation highlights the potential of $Ti_3C_2T_x$/PCL scaffolds with larger SD for long-term applications in neuronal circuitry engineering, as they facilitate the desired alignment and interconnection of neurons.

Cell proliferation on the pristine 3D PCL scaffolds and $Ti_3C_2T_x$/PCL scaffolds with varying concentrations of $Ti_3C_2T_x$ MXene coatings was analyzed over 7 days by quantifying the area covered by live cell fluorescent staining. As shown in Fig. 7, the number of cells proliferating on $Ti_3C_2T_x$ MXene-coated PCL scaffolds surpassed those on pristine PCL scaffolds

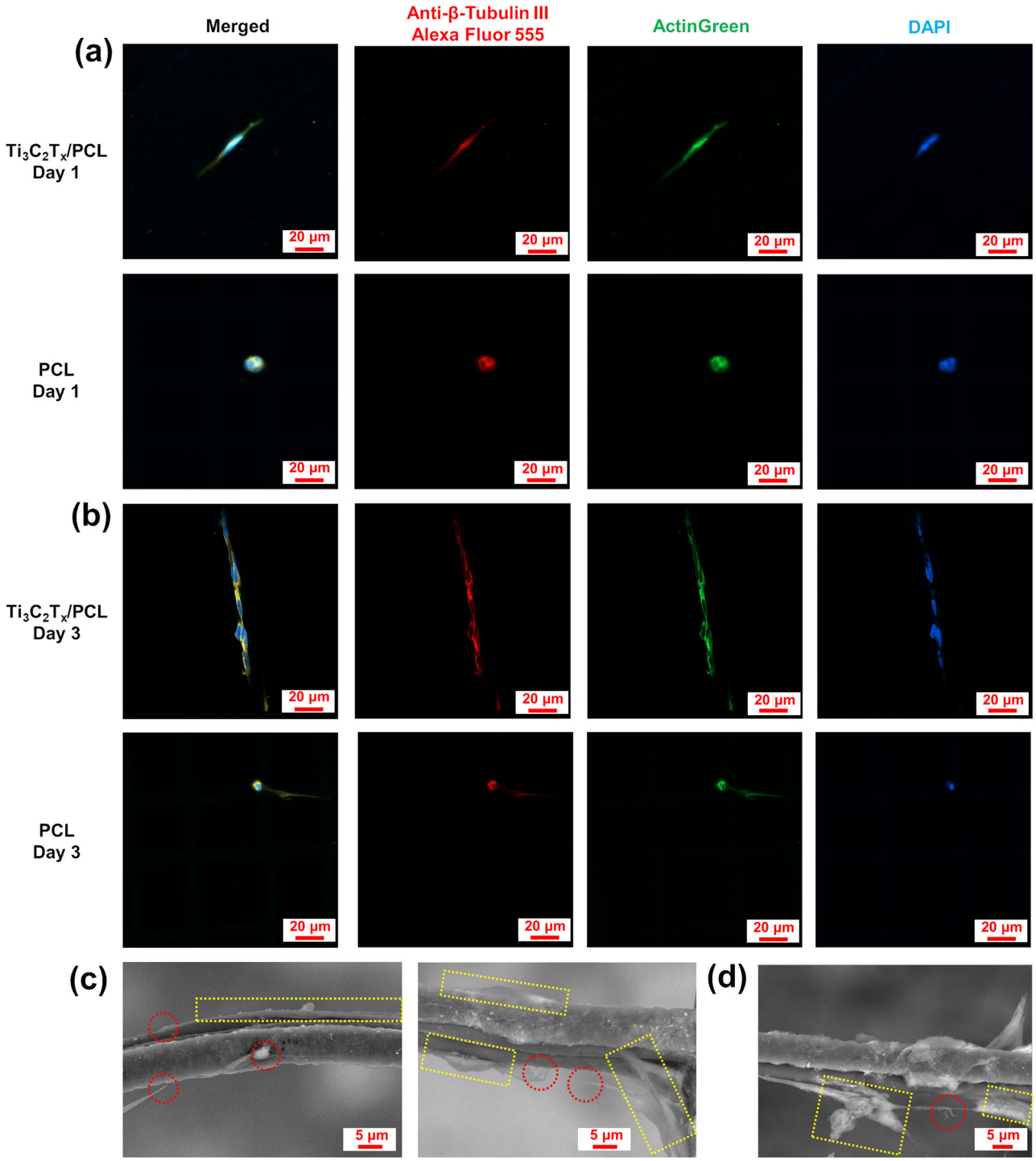

Fig. 5 | Neuronal morphology analysis on the $Ti_3C_2T_x$ MXene (3.0 mg mL^{-1} dispersion) coated PCL and pristine PCL scaffolds. Fluorescence images of immunostained cultures towards dopaminergic lineage induction at **a** Day 1 and **b** Day 3, correspondingly. Neuronal marker β-tubulin III (Alexa Fluor™ 555; red), F-actin (Alexa Fluor™ 488 phalloidin; green), and nuclei [4′,6-diamidino-2-phenylindole (DAPI); blue]. **c** SEM images of neuronal cells on the 3D $Ti_3C_2T_x$/PCL scaffolds with featured cell bodies and growth cones. Red dotted circles highlight the neuronal growth cone structures and yellow dotted squares highlight the neuronal cell bodies. **d** SEM image showing interneuronal connection on the 3D $Ti_3C_2T_x$/PCL scaffold with featured cell bodies and synaptic connection. Red dotted circles highlight the formed synapse between neurons and yellow dotted squares highlight the neuronal cell bodies.

consistently from Day 1 to Day 7, with a generally higher cell count associated with higher concentrations of $Ti_3C_2T_x$ MXene coatings. In particular, the cell numbers on $Ti_3C_2T_x$/PCL scaffolds coated with 3.0 mg mL^{-1} (Day 7) and 15.0 mg mL^{-1} (Day 1 and Day 7) $Ti_3C_2T_x$ MXene dispersions were significantly higher than the cell numbers on pristine 3D PCL scaffolds (Day 1 and Day 7), with the cell count on the 15.0 mg mL^{-1} $Ti_3C_2T_x$ MXene-coated scaffolds being 312 times higher than that on pristine PCL scaffolds (Day 7). The exceptionally high cell count observed can be attributed to the larger cell-supporting area created by the $Ti_3C_2T_x$ MXene coating, which blocked pores in the scaffolds (Supplementary Fig. 3), while the loose adhesion of cells on the pristine PCL scaffolds may also cause cell loss during culture. Conversely, the poor adhesion of cells on pristine PCL scaffolds may

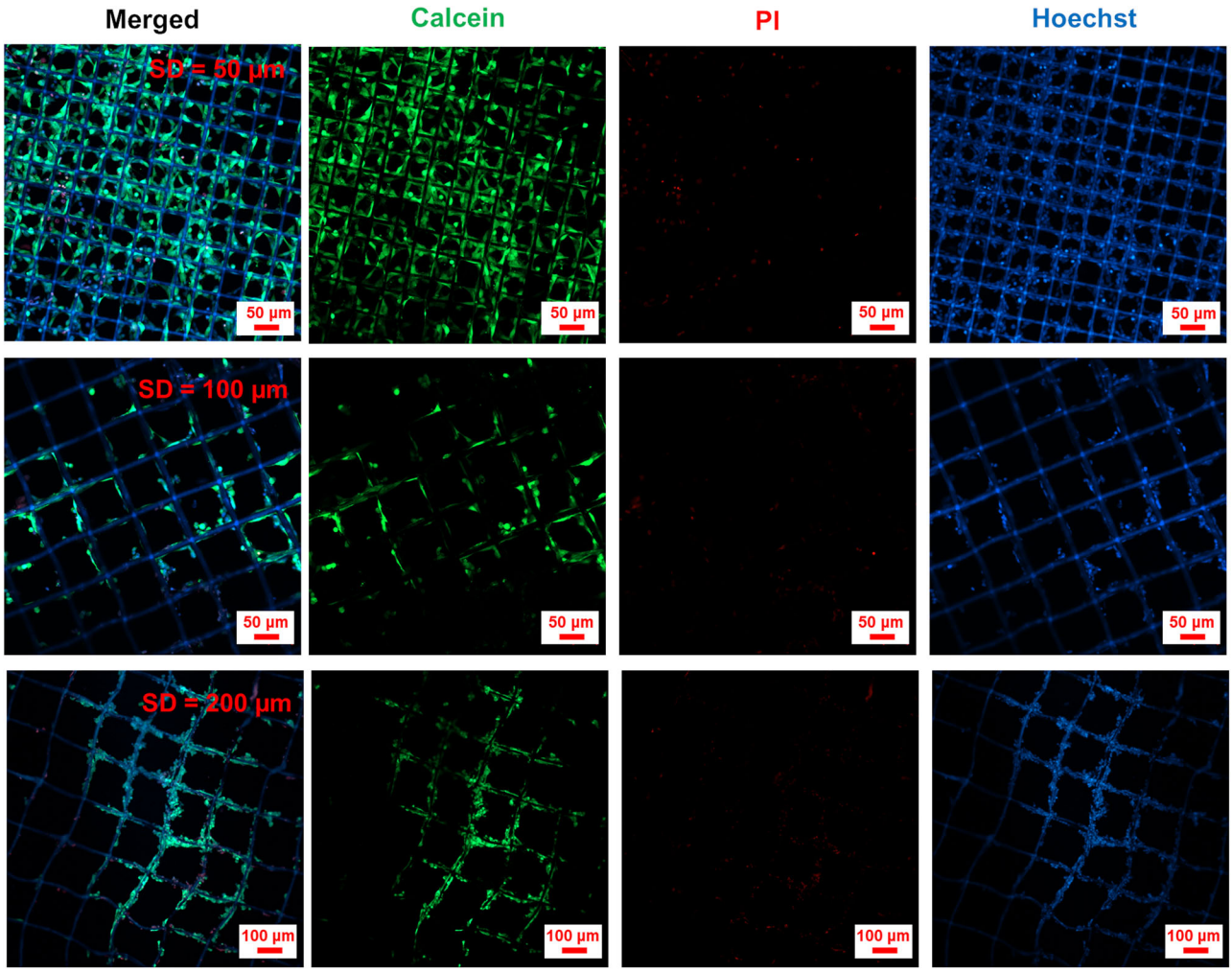

Fig. 6 | Cell viability and morphology on the 3D $Ti_3C_2T_x$/PCL scaffolds with different SDs (50, 100, and 200 μm) after 7-day culture. Fluorescence images of neuronal cells on the 3D $Ti_3C_2T_x$/PCL scaffolds with different SDs. Live cell (Calcein; green), dead cell [propidium iodide (PI); red] and cell nucleus with PCL substrate (Hoechst; blue).

have resulted in cell loss during the culture period. The lack of increase in cell numbers on 0.5 mg mL^{-1} $Ti_3C_2T_x$ MXene-coated scaffolds from Day 1 to Day 7 can be attributed to the low coverage and stability of the coating derived from the highly diluted $Ti_3C_2T_x$ MXene dispersion during cell culture. This limited growing space and caused detachment of cells from the substrate. Statistical analyses further reveal the significant impact of both $Ti_3C_2T_x$ MXene coating concentration [$F(4,20) = 142.65$, $P < 0.01$] and culture time [$F(1,20) = 116.34$, $P < 0.01$] on cell proliferation. Additionally, the interaction between $Ti_3C_2T_x$ MXene coating concentration and culture time was found to be significant [$F(4,20) = 56.75$, $P < 0.01$]. Hence, the $Ti_3C_2T_x$ MXene coating exhibits the potential to provide an enhanced substrate for neuron proliferation.

Photothermal effect in $Ti_3C_2T_x$ MXene and modulating neuronal activity with 3D $Ti_3C_2T_x$/PCL scaffold

$Ti_3C_2T_x$ MXene can convert light to heat efficiently[54], which is critical to trigger the transient capacitive current across the neuronal cell membrane[20,21]. First, we obtained a calibration curve of the resistance change vs. temperature of a MXene film on a glass slide. The natural logarithm of the relative resistance change ($\ln(R_t/R_0)$) was found to be linearly correlated to the reciprocal of temperature ($1/T$) ($\ln(R_t/R_0) = 1.98 \times 10^3\ 1/T - 6.64$; $R^2 = 0.994$; Supplementary Fig. 8), following Arrhenius law. Next, we measured the resistance of this $Ti_3C_2T_x$ MXene sample in the presence of an illumination at a wavelength of 640 nm. An incident intensity of about 4.0×10^2 W mm^{-2} (the incident power was 0.485 mW, the focal laser spot diameter was 1.24 μm) for a duration of 10 s led to a resistance change corresponding to a temperature increase of 3.4 ± 0.7 K in $Ti_3C_2T_x$ MXene, which is similar to other reported results[26]. The intensity is similar to that used for stimulated emission depletion (STED) microscopy[55,56]. Despite the high intensity, the incident light did not appear to have damaged the stimulated cells, which may be due to the fact that the laser spot was scanned rather than held stationary[57].

Finally, we applied the same incident intensity onto a $Ti_3C_2T_x$/PCL scaffold with SH-SY5Y cells. To investigate whether photostimulation can cause neural activity, the cells were loaded with Ca^{2+} dye for imaging Ca^{2+} transients. Ca^{2+} are a second messenger of intracellular signal processing and its transient dynamics reflect cellular activity[26,58]. Since the thermal conductivity of PCL is lower than silicate glass (0.2 W m^{-1} K^{-1} [59] vs. 1.27 W m^{-1} K^{-1} [60]), the induced temperature increase of the $Ti_3C_2T_x$/PCL scaffold could be slightly higher than 3.4 K. As shown in Fig. 8a, b and Supplementary Movie 5, 640 nm laser light induced Ca^{2+} influx of cell on the $Ti_3C_2T_x$/PCL scaffold after illumination of about 17 s with an intensity of 4.0×10^2 W mm^{-2}, while no discernible cellular activity was observed in cells situated on the pristine PCL scaffold (Supplementary Fig. 9a, b and Supplementary Movie 6). These findings show that the MXene coating was required for the photostimulation of neurons on the scaffold, with the temperature increase and optocapacitive effect as the most likely cause. The longer time required to trigger neuronal activity compared to previous work[20] can be attributed to the use of a shorter stimulation wavelength, which is less absorptive by the neurons. Additionally, the heat generated by

the thin layer of $Ti_3C_2T_x$ is easily dissipated through the culture medium and adjacent $Ti_3C_2T_x$ layers in the cell culture environment. Since an optical beam can be focused to micron and sub-micron diameters, photostimulation can enable spatially precise control of cellular activity within the neuron circuits cultured on the scaffold.

Conclusion

In summary, we have presented an effective approach toward active biointerfaces using $Ti_3C_2T_x$ MXene-coated 3D printed scaffolds for facilitating functional tissue engineering and modulation of neural circuits. Neuron growth was guided by the 3D structure of the scaffold, while the $Ti_3C_2T_x$ MXene coating increased the hydrophilicity, cell adhesion, and electrical conductivity of the PCL scaffolds. The optocapacitance-based stimulation was achieved by inducing localized temperature changes in the scaffold of several degrees with red light irradiation, and the photoinduced neural activity was confirmed by Ca^{2+} imaging. This work demonstrates an architecture that combines advanced 3D printing techniques with the application of $Ti_3C_2T_x$ MXene coatings for spatially controlling neuron growth and photostimulation of neural activity. Using holographic light patterns for 2D and 3D photostimulation in combination with scaffolds with more complex structures opens new possibilities for the precise control of neural circuits both in vitro and in vivo.

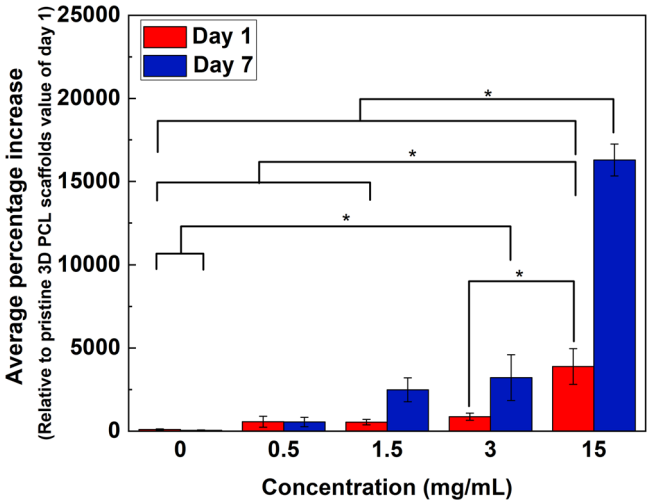

Fig. 7 | Cell proliferation on pristine 3D PCL scaffolds and $Ti_3C_2T_x$/PCL scaffolds coated with various $Ti_3C_2T_x$ MXene concentrations. $Ti_3C_2T_x$ MXene coating improved both neuron adhesion and proliferation on the substrates.

Methods

3D MEW-based printing of PCL

Scaffolds composed of microfibers were 3D printed with polycaprolactone (PCL, average Mn 45,000, Merck, Germany) loaded in a 3 mL metallic cartridge. The printing process was conducted at 65 °C with an air pressure of 70 kPa, a speed of 40 mm s^{-1}, a 24 G nozzle positioned 1.5 mm from the collecting glass slide substrate (VWR, Germany) and an applied voltage of 5.0 kV (3D Discovery Evolution, RegenHU, Switzerland). Rectangular 3D models (35 mm × 15 mm) with varying SDs of 200, 100, and 50 µm, each comprising 6 layers, were designed using BioCAD software (RegenHU, Switzerland) for subsequent 3D printing. PCL scaffolds featuring random patterns were printed with a 50 µm SD, a voltage of 5.5 kV, and a nozzle tip-to-substrate distance of 3 mm. During the printing process, molten PCL was extruded from the cartridge and the generated fibers were formed within the applied electric field. Subsequently, they were deposited and solidified onto the collecting glass slide substrate. To facilitate further measurements and applications, the 3D printed PCL scaffolds were cut into dimensions of 5 mm × 15 mm using a surgical blade (VWR, Germany) and detached from the glass substrate using a 70% EtOH (PanReac AppliChem ITW Reagents, Germany) deionized water (DI water) solution.

Synthesis of $Ti_3C_2T_x$ MXene

$Ti_3C_2T_x$ MXene was synthesized according to the previously reported method[61]. Ti_3AlC_2 (5 g, Carbon-Ukraine Ltd., Ukraine) was mixed with 50 mL ice-cold solution of HCl (12 M, 37 wt.% VWR, Germany), deionized

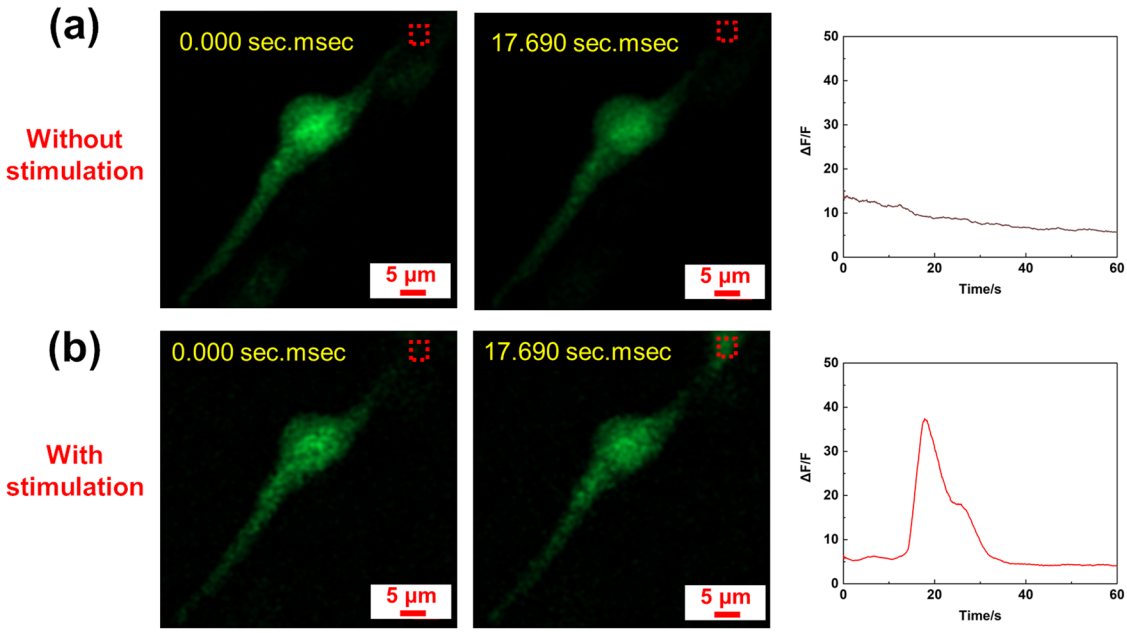

Fig. 8 | Optical modulation of neuronal cell activity on the $Ti_3C_2T_x$/PCL scaffold. **a** Fluorescence image of typical SH-SY5Y cells loaded with calcium ions (Ca^{2+}) indicator at different time points without 640 nm laser stimulation, followed by a corresponding graph showing the relative change in fluorescence intensity of the region of interest (ROI; red dashed square). **b** Fluorescence image of a typical SH-SY5Y cell at different time points with 640 nm laser stimulation, followed by a corresponding graph showing the relative change in fluorescence intensity of the ROI (red dashed square). Stimulation was initiated simultaneously with the imaging process.

Table 1 | Preparation of $Ti_3C_2T_x$ MXene with different concentrations

Ingredient	3.0 mg mL^{-1}	1.5 mg mL^{-1}	0.5 mg mL^{-1}
15.0 mg mL^{-1} MXene	200 μL	100 μL	33 μL
Ethanol	700 μL	700 μL	700 μL
Water	100 μL	200 μL	267 μL

water, and HF (27–29 M, 48–51 wt.%, Alfa Aesar, Germany) with a volumetric ratio of 30:15:5. The mixture in the propylene bottle equipped with PTFE coated magnet bar was stirred at 500 rpm for 1 h at 0 °C, followed by stirring at 35 °C for 24 h. The obtained product was then washed by repeated cycles of centrifugation at relative centrifugal force (RCF) of 2493 × *g*, 10 °C for 10 min, followed by decanting the acidic supernatant and adding fresh deionized water and mixing, until the pH of the supernatant was neutral.

For delamination, the obtained multilayer $Ti_3C_2T_x$ MXene particles from the previous step were reacted with 100 mL aqueous solution of LiCl (1.18 M, 99% Sigma Aldrich, Germany) for 24 h at room temperature (RT, 25 °C), while being stirred at 500 r.p.m. The work-up of the reaction mixture started by centrifugation in the same way as explained above until a very dark black supernatant, containing the delaminated MXene flakes, was formed (usually after four times of washing/centrifugation). From this point onward, the supernatants were collected after each centrifugation until the supernatant was no longer dark black and turned into an almost transparent green solution. The collected supernatants were combined and concentrated by high-speed centrifugation at RCF 9420 × *g*, 10 °C, 20 min. The obtained precipitates (containing the MXene flakes) were mixed with 200 mL of deionized water to produce a concentration of 15.0 mg mL^{-1}, as measured by gravimetric vacuum filtration.

Coating of $Ti_3C_2T_x$ MXene

$Ti_3C_2T_x$ MXene aqueous dispersion was diluted with EtOH to obtain $Ti_3C_2T_x$ MXene 70% EtOH dispersion for coating to achieve improved wetting property for the pristine PCL scaffolds. In all, 3.0, 1.5, and 0.5 mg mL^{-1} $Ti_3C_2T_x$ MXene 70% EtOH dispersion were prepared by diluting the 15.0 mg mL^{-1} $Ti_3C_2T_x$ MXene water dispersion through adding specific amounts of ethanol, as shown in Table 1. DI water was used in all the experiments and all the obtained dispersions were ultrasonicated (Sonorex digitec; Bandelin, Germany) for 30 min to assist the $Ti_3C_2T_x$ MXene uniform dispersion. For 15.0 mg mL^{-1} $Ti_3C_2T_x$ MXene aqueous dispersion coating, the substrate was detached from the substrate with 10 μL 70% to EtOH and the extra solvent was removed by a Kimwipe tissue paper (Kimberly-Clark, USA), followed by dropping 10 μL 15.0 mg mL^{-1} $Ti_3C_2T_x$ MXene aqueous dispersion with subsequent overturning several times by tweezers, similar to previous reported method[45]. For EtOH containing dispersion, 10 μL $Ti_3C_2T_x$ MXene 70% EtOH was deposited onto the PCL scaffold and the dispersion spread automatically, only needing tweezers to assist uniform wetting. The coated samples were dried on a hotplate (VWR, Germany) at 50 °C for 2 min in a fume hood (Waldner, Germany).

Contact angle measurement

The wettability of the structures was determined by using the sessile drop measurement on an optical tensiometer (Biolin Scientific Theta Lite, Finland). A 4 μL DI water or 70% EtOH droplet was placed on the tested structures placed on the measuring stage and imaged with a high-speed camera for 10 s at an imaging speed of 51 frames per second. The results were analyzed with the Young–Laplace method.

Electrical resistance measurement

Sheet resistance of the $Ti_3C_2T_x$ MXene-coated scaffolds were measured for evaluation of coating quality according to previously reported method[32]. Two copper electrodes with a length of *L* were placed parallelly on the rectangular $Ti_3C_2T_x$ MXene-coated PCL scaffolds (length: 15 mm and width: 5 mm) with a distance of *D*. A digital multimeter (Agilent 34401A, USA) was used for the measurement of resistance [*R* (Ω)] between the two copper electrodes and the sheet resistance of MXene-coated PCL scaffold [ρ (Ω □$^{-1}$)] was defined as: $\rho = R \times \frac{L}{D}$.

Scanning electron microscopy

Morphology of MAX phase Ti_3AlC_2 and $Ti_3C_2T_x$ MXene was imaged on a field emission SEM (FESEM, Zeiss Gemini 500) with the InLens detector. Max phase powder particles and etched MXene particles were directly imaged on a conductive carbon tape. $Ti_3C_2T_x$ MXene was prepared by the following procedures. A diluted aqueous dispersion (0.1 mg mL^{-1}) of delaminated $Ti_3C_2T_x$ MXene flakes was spin-coated on a diced silicon wafer substrate. After drying in the vacuum oven at RT, 10 mBar for 8 h, the substrate was glued to the SEM stub with conductive silver lacquer.

Morphology of 3D PCL scaffolds and 3D $Ti_3C_2T_x$/PCL scaffolds were characterized with a tabletop SEM (Hitachi TM4000Plus, Japan). For cell containing samples, a fixation of the samples was first carried out in paraformaldehyde fixative solution (PFS; Alfa Aesar, USA) for 30 min with subsequent washing in phosphate-buffered saline (PBS; Thermal Fisher, Germany) solution for 3 times, and then the characterization by the SEM was assisted with an ultra coolstage at −30 °C (Deben, UK).

X-ray diffraction

Ex situ powder XRD pattern of MAX Phase Ti_3AlC_2 powder was obtained on an X-ray diffractometer (Aeris Research Edition, Malvern Panalytical Company) using Cu-Kα radiation (λ = 0.15418 nm) at 40 kV and 15 mA at RT in reflection geometry.

Culture and differentiation of human SH-SY5Y cells

For the sterilization of samples before cell culture, 3D printed PCL and three-time-coated $Ti_3C_2T_x$/PCL scaffolds were immersed in a 70% EtOH solution for 2 h, and then dried under UV illumination in a biological safety cabinet (BSC; Kojair, Finland) for 1 h. Subsequently, the scaffolds were incubated in culture medium (CM) overnight before cell seeding and maintained in a humidified cell culture incubator (5% CO_2 and 37 °C; Binder, Germany). SH-SY5Y cells (Elabscience, China) were seeded on both pristine 3D PCL and $Ti_3C_2T_x$/PCL scaffolds with a cell density of 3×10^5 cells cm^{-2}, with the medium refreshed every 2 days. The CM consisted of Dulbecco's Modified Eagle's Medium/Nutrient Mixture F-12 (DMEM/F-12; HyClone, USA), 15% (v/v) heat inactivated newborn bovine calf serum (HyClone, USA), 1% (v/v) penicillin-streptomycin (10,000 U mL^{-1}; ThermoFisher Scientific, Germany). The differentiation medium (DM) was prepared by supplementing the CM with 10 μM retinoic acid (RA; Merck, Germany).

Viability staining

For cell viability, distribution and proliferation evaluation, 8 μg mL^{-1} Calcein AM (Merck, Germany), 4 μg mL^{-1} PI (Merck, Germany), and 12 mg mL^{-1} Hoechst 33342 (Miltenyi Biotec, Germany) were used to stain the live cells, dead cells and nuclei, respectively. Briefly, samples were incubated with Calcein AM for 15 min in an incubator, following with addition of PI and Hoechst for an additional 15 min incubation in an incubator. After samples washing with fresh CM, images were obtained with a confocal microscope (LSM 900) (Zeiss, Germany) and analyzed with Zen software (Zeiss, Germany). For viability and proliferation analysis, the area of stained live/dead cells was extracted by ImageJ/Fiji software[62].

Immunofluorescence staining

Samples were washed in PBS solution with subsequent fixation in PFS for 30 min at RT after 2-day culture in CM, before and after 3 days culture in DM. Fixed samples were rinsed 3 times in PBS solution, before being blocked and permeabilized by a PBS solution supplemented with 10% (v/v) horse serum (HS; MP Biomedicals, USA) and 0.3% (v/v) Triton X-100 (Merck, Germany) at RT. After 3 times washing in PBS, samples were incubated in a 10% (v/v) HS PBS solution supplemented with primary mouse anti-β-tubulin III antibody (1:100; Merck, Germany) overnight at

4 °C. Thereafter, samples were washed in PBS for 3 times and Alexa Fluor™ 555 conjugated secondary goat anti-mouse IgG antibody (1:100; BioLegend, USA) was added for immunostaining in the dark for 2 h at RT. F-actin and nuclei were stained by Alexa Fluor™ 488 phalloidin (ThermoFisher Scientific, Germany) and DAPI (Merck, Germany) in the dark for 1 h at RT, respectively. After samples washing in PBS, ProLong™ glass antifade mountant (ThermoFisher Scientific, Germany) was used to mount the samples on a glass slide before imaging. Images were obtained with Zeiss LSM 900 and analyzed with Zeiss Zen software.

Photothermal effect studies

Material electrical resistance changes with temperature by following Arrhenius relationship[26]

$$\ln\left(\frac{R_t}{R_0}\right) = \frac{a}{T} + b,$$

where R_t is the measured electrical resistance at temperature T, R_0 is the measured electrical resistance at temperature 303.15 K (30 °C), a is the slope of the curve and b is the curve intercept. The MXene electrode was prepared by adding 10 μL 10 mg mL^{-1} MXene water solution on the glass slide with a 2 mm trench made by two parallel scotch tape (3M, USA) and dried on a 50 °C hot plate (VWR, Germany) for 5 min in the fume hood. The electrode temperature was controlled by submerging in 70 °C PBS solution with a P4010 thermal meter (Dostmann electronic, Germany) for temperature monitoring and a 34401A digit multimeter (Agilent, USA) for electrical resistance measurement. For the photothermal effect measurement of the MXene sample, the fluorescent latex beads (2 μm, fluorescent red; Merck, Germany) were diluted by 1000 times and added in the MXene electrode to assist in finding the focal plane when applying photo stimulation. Confocal microscope (LSM 900) (Zeiss, Germany) was used for applying laser stimulation and the laser power was measured by an 843-R power meter (Newport, USA). The laser focus spot size was estimated with the following equation:

$$d_0 = \frac{4\lambda f M^2}{\pi D_0},$$

where d_0 is the focal laser spot diameter, λ is the wavelength, M^2 is the beam quality parameter, f is the focal length, and D_0 is the input beam diameter. The diameter is 1.24 μm.

Calcium imaging

Samples were loaded with 5 μM Fluo-4 AM (ThermoFisher Scientific, Germany) in CM for 30 min in a cell culture incubator (37 °C and humidified 5% CO_2), while 0.02% (w/v) Plu was added to assist the calcium dye dispersion in CM, following the manufacturer's instructions. After loading, samples were washed in fresh CM and imaged using a confocal microscope (Zeiss LSM 900) equipped with a mounted incubator (XLmulti S2 DARK, Germany). The 488 nm and 640 nm lasers were turned on during the imaging process, with a line scan frequency of ~3 KHz and a pixel dwell time of ~2 μs, using bidirectional scanning. The pixel size is 397 nm for the cell on the MXene-coated scaffold imaging, while it is 248 nm for the cell on the pristine scaffold. ImageJ/Fiji software was used for acquired image and movie processing. Background fluorescence was subtracted prior to fluorescence change analysis of ROIs.

Statistical analysis

All the obtained quantitative data were demonstrated as mean ± standard deviation and measurements were executed in triplicate. Two-way analysis of variance (ANOVA, Bonferroni post hoc test) was performed with a significance level set of <0.05 if homogeneity of variance (Brown–Forsythe test) was satisfied (>0.05). Otherwise, the significance level was set to <0.01. All the statistical analyses were carried out by using OriginPro 2019 software (OriginLab, USA).

Reporting summary

Further information on research design is available in the Nature Portfolio Reporting Summary linked to this article.

Data availability

The data that support this work will be made available upon reasonable request.

Received: 12 December 2023; Accepted: 11 April 2024;
Published online: 24 April 2024

References

1. Abeles, M. *Corticonics: Neural Circuits of the Cerebral Cortex* (Cambridge University Press, 1991).
2. Chambers, A. R. & Rumpel, S. A stable brain from unstable components: emerging concepts and implications for neural computation. *Neuroscience* **357**, 172–184 (2017).
3. Maass, W., Papadimitriou, C., Vempala, S. & Legenstein, R. in *Computing and Software Science* (eds Steffen, B. & Woeginger, G.) 184–199 (Springer, 2019).
4. Chan, D. et al. Induction of specific brain oscillations may restore neural circuits and be used for the treatment of Alzheimer's disease. *J. Intern. Med.* **290**, 993–1009 (2021).
5. National Academy of Sciences (US). *International Animal Research Regulations: Impact on Neuroscience Research: Workshop Summary. The National Academies Collection: Reports Funded by National Institutes of Health* (National Academies Press (US), 2012).
6. Offenhäusser, A. et al. Microcontact printing of proteins for neuronal cell guidance. *Soft Matter* **3**, 290–298 (2007).
7. Onoe, H., Kato-Negishi, M., Itou, A. & Takeuchi, S. Differentiation induction of mouse neural stem cells in hydrogel tubular microenvironments with controlled tube dimensions. *Adv. Healthc. Mater.* **5**, 1104–1111 (2016).
8. Abu-Rub, M. T. et al. Nano-textured self-assembled aligned collagen hydrogels promote directional neurite guidance and overcome inhibition by myelin associated glycoprotein. *Soft Matter* **7**, 2770–2781 (2011).
9. Kato-Negishi, M., Tsuda, Y., Onoe, H. & Takeuchi, S. A neurospheroid network-stamping method for neural transplantation to the brain. *Biomaterials* **31**, 8939–8945 (2010).
10. Pautot, S., Wyart, C. & Isacoff, E. Y. Colloid-guided assembly of oriented 3D neuronal networks. *Nat. Methods* **5**, 735–740 (2008).
11. Rose, J. C. et al. Nerve cells decide to orient inside an injectable hydrogel with minimal structural guidance. *Nano Lett.* **17**, 3782–3791 (2017).
12. Ye, W. et al. 3D printing of gelatin methacrylate-based nerve guidance conduits with multiple channels. *Mater. Des.* **192**, 108757 (2020).
13. Broguiere, N. et al. Morphogenesis guided by 3D patterning of growth factors in biological matrices. *Adv. Mater.* **32**, 1908299 (2020).
14. Pisanello, F., Sileo, L. & De Vittorio, M. Micro- and nanotechnologies for optical neural interfaces. *Front. Neurosci*. **10**, 70 (2016).
15. Häusser, M. Optogenetics: the age of light. *Nat. Methods* **11**, 1012–1014 (2014).
16. Obien, M. E. J., Deligkaris, K., Bullmann, T., Bakkum, D. J. & Frey, U. Revealing neuronal function through microelectrode array recordings. *Front. Neurosci*. **8**, 423 (2015).
17. Gilbert, F., Harris, A. R. & Kapsa, R. M. I. Controlling brain cells with light: ethical considerations for optogenetic clinical trials. *AJOB Neurosci.* **5**, 3–11 (2014).
18. Ferguson, M., Sharma, D., Ross, D. & Zhao, F. A critical review of microelectrode arrays and strategies for improving neural interfaces. *Adv. Healthc. Mater.* **8**, 1900558 (2019).
19. Carvalho-de-Souza, J. L., Pinto, B. I., Pepperberg, D. R. & Bezanilla, F. Optocapacitive generation of action potentials by microsecond laser pulses of nanojoule energy. *Biophys. J.* **114**, 283–288 (2018).
20. Shapiro, M. G., Homma, K., Villarreal, S., Richter, C.-P. & Bezanilla, F. Infrared light excites cells by changing their electrical capacitance. *Nat. Commun.* **3**, 736 (2012).

21. Plaksin, M., Shapira, E., Kimmel, E. & Shoham, S. Thermal transients excite neurons through universal intramembrane mechanoelectrical effects. *Phys. Rev. X* **8**, 011043 (2018).
22. Wäldchen, S., Lehmann, J., Klein, T., van de Linde, S. & Sauer, M. Light-induced cell damage in live-cell super-resolution microscopy. *Sci. Rep.* **5**, 15348 (2015).
23. Emon, M. A. B. et al. Dose-independent threshold illumination for non-invasive time-lapse fluorescence imaging of live cells. *Extreme Mech. Lett*. **46**, 101249 (2021).
24. Dubois, A. et al. Optical and thermal simulations for the design of optodes for minimally invasive optogenetics stimulation or photomodulation of deep and large cortical areas in non-human primate brain. *J. Neural Eng.* **15**, 065004 (2018).
25. Rastogi, S. K. et al. Remote nongenetic optical modulation of neuronal activity using fuzzy graphene. *Proc. Natl Acad. Sci. USA* **117**, 13339–13349 (2020).
26. Wang, Y. et al. $Ti_3C_2T_x$ MXene flakes for optical control of neuronal electrical activity. *ACS Nano* **15**, 14662–14671 (2021).
27. Shah, S., Solanki, A. & Lee, K. B. Nanotechnology-based approaches for guiding neural regeneration. *Acc. Chem. Res.* **49**, 17–26 (2016).
28. Xu, D., Li, Z., Li, L. & Wang, J. Insights into the photothermal conversion of 2D MXene nanomaterials: synthesis, mechanism, and applications. *Adv. Funct. Mater.* **30**, 2000712 (2020).
29. El-Demellawi, J. K., Lopatin, S., Yin, J., Mohammed, O. F. & Alshareef, H. N. Tunable multipolar surface plasmons in 2D $Ti_3C_2T_x$ MXene flakes. *ACS Nano* **12**, 8485–8493 (2018).
30. Nan, L.-P. et al. $Ti_3C_2T_x$ MXene-coated electrospun PCL conduits for enhancing neurite regeneration and angiogenesis. *Front. Bioeng. Biotechnol*. **10**, 850650 (2022).
31. Thijssen, Q., Parmentier, L., Augustyniak, E., Mouthuy, P.-A. & Van Vlierberghe, S. From chain growth to step growth polymerization of photoreactive poly-ε-caprolactone: the network topology of bioresorbable networks as tool in tissue engineering. *Adv. Funct. Mater.* **32**, 2108869 (2022).
32. Li, J., Liu, X., Crook, J. M. & Wallace, G. G. Development of a porous 3D graphene-PDMS scaffold for improved osseointegration. *Colloids Surf. B* **159**, 386–393 (2017).
33. Wychowaniec, J. K. et al. Unique cellular network formation guided by heterostructures based on reduced graphene oxide - $Ti_3C_2T_x$ MXene hydrogels. *Acta Biomater.* **115**, 104–115 (2020).
34. Xiong, K. et al. Functional group effects on the photoelectronic properties of MXene (Sc_2CT_2, T = O, F, OH) and their possible photocatalytic activities. *Sci. Rep.* **7**, 15095 (2017).
35. Ibragimova, R., Erhart, P., Rinke, P. & Komsa, H.-P. Surface functionalization of 2D MXenes: trends in distribution, composition, and electronic properties. *J. Phys. Chem. Lett.* **12**, 2377–2384 (2021).
36. Thapaliya, B. P. et al. Fluorination of MXene by elemental F_2 as electrode material for lithium-ion batteries. *ChemSusChem* **12**, 1316–1324 (2019).
37. Zhao, X. et al. Antioxidants unlock shelf-stable $Ti_3C_2T_x$ (MXene) nanosheet dispersions. *Matter* **1**, 513–526 (2019).
38. Xue, J., Wu, T., Dai, Y. & Xia, Y. Electrospinning and electrospun nanofibers: methods, materials, and applications. *Chem. Rev.* **119**, 5298–5415 (2019).
39. Brown, T. D., Dalton, P. D. & Hutmacher, D. W. Direct writing by way of melt electrospinning. *Adv. Mater.* **23**, 5651–5657 (2011).
40. Dalton, P. D. Melt electrowriting with additive manufacturing principles. *Curr. Opin. Biomed. Eng.* **2**, 49–57 (2017).
41. Wunner, F. M. et al. Melt electrospinning writing of highly ordered large volume scaffold architectures. *Adv. Mater.* **30**, 1706570 (2018).
42. Robinson, T. M., Hutmacher, D. W. & Dalton, P. D. The next frontier in melt electrospinning: taming the jet. *Adv. Fun. Mater.* **29**, 1904664 (2019).
43. Qin, X. et al. Surface modification of polycaprolactone scaffold with improved biocompatibility and controlled growth factor release for enhanced stem cell differentiation. *Front. Bioeng. Biotechnol*. **9**, 802311 (2022).
44. Sun, L. et al. Tailoring materials with specific wettability in biomedical engineering. *Adv. Sci.* **8**, 2100126 (2021).
45. Li, J., Liu, X., Tomaskovic-Crook, E., Crook, J. M. & Wallace, G. G. Smart graphene-cellulose paper for 2D or 3D "origami-inspired" human stem cell support and differentiation. *Colloids Surf. B* **176**, 87–95 (2019).
46. Seok, S.-H. et al. Synthesis of high quality 2D carbide MXene flakes using a highly purified MAX precursor for ink applications. *Nanoscale Adv.* **3**, 517–527 (2021).
47. Shahzad, F., Iqbal, A., Kim, H. & Koo, C. M. 2D transition metal carbides (MXenes): applications as an electrically conducting material. *Adv. Mater.* **32**, 2002159 (2020).
48. Kumar, V. et al. MXene reinforced thermosetting composite for lightning strike protection of carbon fiber reinforced polymer. *Adv. Mater. Interfaces* **8**, 2100803 (2021).
49. Metwally, S. et al. Surface potential and roughness controlled cell adhesion and collagen formation in electrospun PCL fibers for bone regeneration. *Mater. Des.* **194**, 108915 (2020).
50. Firestein, K. L. et al. Young's modulus and tensile strength of Ti_3C_2 MXene nanosheets as revealed by in situ tem probing, afm nanomechanical mapping, and theoretical calculations. *Nano Lett.* **20**, 5900–5908 (2020).
51. Zhou, B. et al. Flexible, robust, and multifunctional electromagnetic interference shielding film with alternating cellulose nanofiber and MXene layers. *ACS Appl. Mater. Interfaces* **12**, 4895–4905 (2020).
52. Domingos, M. et al. Improved osteoblast cell affinity on plasma-modified 3D extruded PCL scaffolds. *Acta Biomater.* **9**, 5997–6005 (2013).
53. Lowery, L. A. & Vactor, D. V. The trip of the tip: understanding the growth cone machinery. *Nat. Rev. Mol. Cell Biol.* **10**, 332–343 (2009).
54. Li, R., Zhang, L., Shi, L. & Wang, P. MXene Ti_3C_2: an effective 2D light-to-heat conversion material. *ACS Nano* **11**, 3752–3759 (2017).
55. Schermelleh, L. et al. Super-resolution microscopy demystified. *Nat. Cell Biol.* **21**, 72–84 (2019).
56. Kilian, N. et al. Assessing photodamage in live-cell STED microscopy. *Nat. Methods* **15**, 755–756 (2018).
57. Boudreau, C. et al. Excitation light dose engineering to reduce photo-bleaching and photo-toxicity. *Sci. Rep.* **6**, 30892 (2016).
58. Peng, B. et al. A neuron-readable artificial photoreceptor composed of photodeformable liquid crystal polymers and piezoelectric materials. *Adv. Funct. Mater.* **33**, 2214172 (2023).
59. Tian, H., Wu, F., Chen, P., Peng, X. & Fang, H. Microwave-assisted in situ polymerization of polycaprolactone/boron nitride composites with enhanced thermal conductivity and mechanical properties. *Polym. Int.* **69**, 635–643 (2020).
60. Rahbar, M., Han, M., Xu, S., Zobeiri, H. & Wang, X. Development of differential thermal resistance method for thermal conductivity measurement down to microscale. *Int. J. Heat Mass Transf.* **202**, 123712 (2023).
61. Shuck, C. E. et al. Scalable synthesis of $Ti_3C_2T_x$ MXene. *Adv. Eng. Mater.* **22**, 1901241 (2020).
62. Schindelin, J. et al. Fiji: an open-source platform for biological-image analysis. *Nat. Methods* **9**, 676–682 (2012).

Acknowledgements

Financial support of the Max Planck Society is gratefully acknowledged. The authors thank Dr. Davood Sabaghi for support with the XRD measurements. J.L. would like to acknowledge Mr. Fu-Der Chen, Dr. Andrei Stalmashonak, and Mr. Frank Weiß for technical support.

Author contributions

J.L., W.D.S., X.F. and J.K.S.P. conceived the study and designed the experiments. P.H., J.L., and A.S.N. carried out the synthesis and analysis of MXene solutions. J.L. and X.M. performed the 3D printing experiments. J.L., K.M.D. and M.G.K.B. conducted cell experiments. J.L., T.L. and J.K.S.P. performed and analyzed the stimulation experiments. All authors contributed to the paper and approved the submitted version.

Funding
Open Access funding enabled and organized by Projekt DEAL.

Competing interests
The authors declare no competing interests.

Additional information
Supplementary information The online version contains supplementary material available at https://doi.org/10.1038/s43246-024-00503-6.

Correspondence and requests for materials should be addressed to Jianfeng Li or Joyce K. S. Poon.

Peer review information *Communications Materials* thanks the anonymous reviewers for their contribution to the peer review of this work. Primary handling editor: Jet-Sing Lee. A peer review file is available.

Reprints and permissions information is available at http://www.nature.com/reprints

Publisher's note Springer Nature remains neutral with regard to jurisdictional claims in published maps and institutional affiliations.

Open Access This article is licensed under a Creative Commons Attribution 4.0 International License, which permits use, sharing, adaptation, distribution and reproduction in any medium or format, as long as you give appropriate credit to the original author(s) and the source, provide a link to the Creative Commons licence, and indicate if changes were made. The images or other third party material in this article are included in the article's Creative Commons licence, unless indicated otherwise in a credit line to the material. If material is not included in the article's Creative Commons licence and your intended use is not permitted by statutory regulation or exceeds the permitted use, you will need to obtain permission directly from the copyright holder. To view a copy of this licence, visit http://creativecommons.org/licenses/by/4.0/.

© The Author(s) 2024